Supporting Information

Component Matters: Paving the Roadmap Toward Enhanced Electrocatalytic Performance of Graphitic C_3N_4-Based Catalysts *via* Atomic Tuning

Zengxia Pei,† Jingxing Gu,† Yukun Wang, Zijie Tang, Zhuoxin Liu, Yan Huang, Yang Huang, Jingxiang Zhao, Zhongfang Chen and Chunyi Zhi**

Z. Pei, Y. Wang, Z. Tang, Z. Liu, Y. Huang, Dr. C. Zhi

Department of Physics and Materials Materials Science
City University of Hong Kong
83 Tat Chee Avenue, Kowloon, Hong Kong 999077, China
E-mail: cy.zhi@cityu.edu.hk

J. Gu, Dr. J. Zhao, Prof. Z. Chen
Department of Chemistry
The Institute for Functional Nanomaterials, University of Puerto Rico
Rio Piedras Campus, San Juan, PR 00931, USA
E-mail: zhongfangchen@gmail.com

Dr. Y. Huang
College of Materials Science and Engineering, Shenzhen University,
Shenzhen 518000, China.

Dr. C. Zhi
Shenzhen Research Institute, City University of Hong Kong
High-Tech Zone, Nanshan District, Shenzhen 518057, China

Density Functional Theory (DFT) Computations

All the spin-polarized[1, 2] and van der Waals interaction corrected[3] density functional theory (DFT) computations were carried out by the Dmol[3] code. The electron exchange-correlation functional was treated using generalized gradient approximation (GGA) in the form proposed by Perdew, Burke and Ernzerhof (PBE) [4] , and the double numerical plus polarization (DNP) basis set was employed. A convergence criterion of 10^{-6} a.u. was adopted when doing self-consistent field (SCF) computaitons on the total energy and electronic computations. To simulate a H_2O solvent environment, we used the conductor-like screen model (COSMO) during the whole process,[5] where the dielectric constant was set as 78.54.

The optimized pristine graphitic C_3N_4 supercell is rhombic. We set the *x* and *y* directions parallel to the plane with the cell parameters as a=b=7.13 Å, and the *z* direction is perpendicular to the plane with a vacuum layer of 16.13 Å. We constructed doped C_3N_4 monolayers at the doping concentration of 7.14 at%, which corresponds to one dopant in a supercell. All the computations and discussions are based on this doping centration unless mentioned otherwise. The Brillouin zone was sampled with a 5 × 5 × 1 k points setting for geomtry optimizations, and a 15 × 15 × 1 grid was used for electronic structure computations. The charge transfer was evaluated by the Hirshfeld population analysis method.[6]

HER Computations: to theoretically evaluate the performance of an HER catalyst, we computed the Gibbs free energy change (ΔG_{H^*}) for a hydrogen atom absorbed onto the catalyst's surface. The ΔG_{H^*} was calculated as:

$$\Delta G_{H^*} = \Delta E_{H^*} + \Delta E_{ZPE} - T\Delta S_{H^*} \quad (1)$$

where ΔE_{H^*} is the hydrogen absorption energy, ΔE_{ZPE} and ΔS_{H^*} are the difference of zero-point energy and the difference of entropy between the adsorbed hydrogen and hydrogen in the gas phase, respectively, and T is set to 298.15 K. After some approximations and corrections,[7] formula (1) could be simplified as formula (2):

$$\Delta G_{H^*} = \Delta E_{H^*} + 0.24\ \text{eV} \quad (2)$$

The absorption energy for hydrogen (ΔE_{H^*}) bonding to the doped C_3N_4 was defined as:

$$\Delta E_{H^*} = E_{H\text{-}Cat} - E_{Cat} - 1/2E_{H2} \quad (3)$$

where $E_{H\text{-}Cat}$ is the total energy of the doped C_3N_4 sheet with absorbed hydrogen atom, E_{Cat} is the total energy of the doped C_3N_4 sheet, and E_{H2} is the energy of a hydrogen molecule in the gas phase.

ORR Computations: our experiments were operated under alkaline condition (pH = 13), the associate $4e^-$ overwhelming ORR process, $O_2 + 2H_2O(l) + 4e^- \rightarrow 4OH^-$, has been proved by detecting the HO_2^- yield. Thus, the mechanism can be written as:

$$O_2(g) + H_2O(l) + e^- \rightarrow HOO^* + OH^- \quad (4a)$$

$$HOO^* + e^- \rightarrow O^* + OH^- \quad (4b)$$

$$O^* + H_2O(l) + e^- \rightarrow HO^* + OH^- \quad (4c)$$

$$HO^* + e^- \rightarrow OH^- \quad (4d)$$

where the * represents the active site.

Hereby, we computed the free energy change of each reaction step based on the standard hydrogen electrode (SHE) model.[8] The free energy change for each step is defined as ΔG:

$$\Delta G = \Delta E + \Delta E_{ZPE} - T\Delta S + \Delta G_{pH} + \Delta G_U \quad (5)$$

where ΔE is the reaction energy obtained from the DFT calculations directly, E_{ZPE} is the zero-point energy, and ΔS is the difference in entropy, which is neglected for those intermediates here. ΔG_{pH} is a correction related to pH, computed by $\Delta G_{pH} = k_B T \times \ln 10 \times pH$, where k_B is the Boltzmann constant. $\Delta G_U = neU$, where n is the number of electrons transferred during the reaction step and U is the electrode potential. We set the standard hydrogen electrode (SHE) as the reference, where $H^+(aq) + e^- = 1/2H_2(g)$, and its free energy change is 0. Some thermodynamic data, e.g. entropies and zero point energies referred to the handbook.[9] These data are used to construct the Gibbs free energy of H_2 gas molecule

and H_2O gas molecule at a pressure of 0.035 bar. Then the Gibbs free energy of $H_2O(l)$ is obtained using the free energy of $H_2O(g)$ at 0.035 bar, in which pressure they are in equilibrium to each other. Considering that the equilibrium potential for the half reaction $O_2(g) + 4H^+ + 4e^- = 2H_2O(l)$ under the standard condition is 1.23 V, the free energy of $O_2(g)$ was derived as $G_{O2(g)} = 2G_{H2O(l)} - 2G_{H2(g)} + 4.92$ eV. The free energies of other products and intermediates were computed by DFT method. The equilibrium reduction potential U^0 for O_2 to OH^- at pH = 13 is 0.46 V versus SHE following the $4e^-$ pathway.[10]

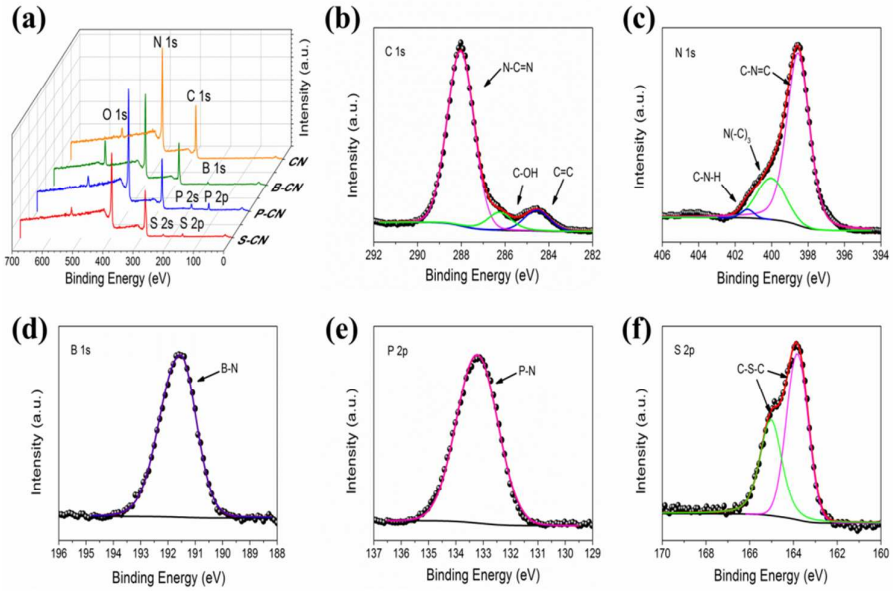

Figure S1. XPS analyses of different samples: (a) survey spectra of different X-CN and bare g-C_3N_4 samples; (b) C 1s and (c) N 1s high resolution spectra recorded from the bare g-C_3N_4 sample; (d) B 1s ,(e) P 2p ,(f) S 2p core spectra from the B-CN, P-CN and S-CN samples, respectively.

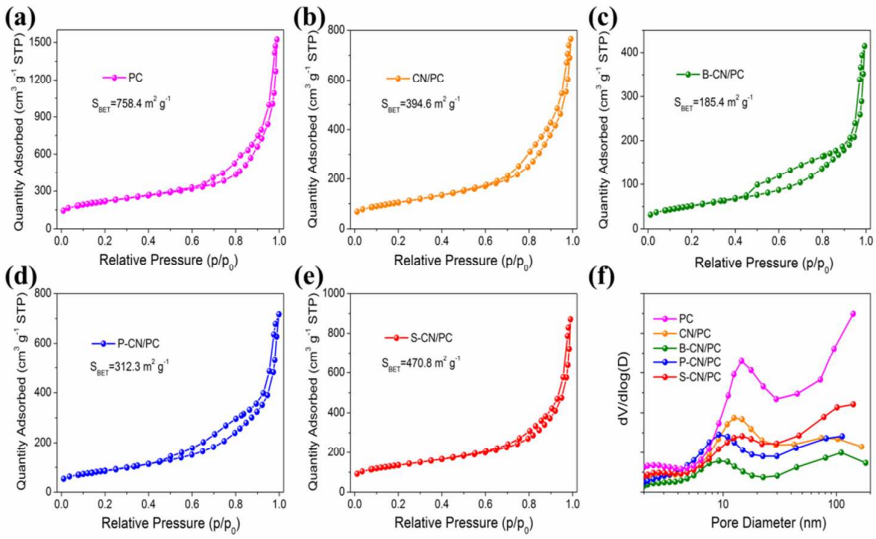

Figure S2. N_2 adsorption/desorption isotherms of (a) bare porous carbon substrate, (b) CN/PC, (c) B-CN/PC, (d) P-CN/PC, (e) S-CN/samples; their corresponding specific surface areas are also given. (f) Pore diameter distribution of all samples.

Note: The carbon substrate has a hierarchical porous structure. The micro- and meso-architecture is reasonably from the leaching of small molecules during the pyrolysis process, while the macro-pore is evidently introduced by the silica template. Considering the deliberately introduced macro-pores, the carbon substrate is named as macroporous carbon (PC) in the text. Also note that the dopant-induced texture difference could affect the nano-architecture of the X-CN/PC samples, from which the B/P doped composites have smaller parameters (specific surface area, pore diameter) compared with the other two, according with the TEM morphology observations in Figure 1e-l. The decreased surface area and the gradually dwindling pore diameter also indicate the filling effect of the *in situ* polymerized g-C_3N_4 species in the pores of the PC substrate.

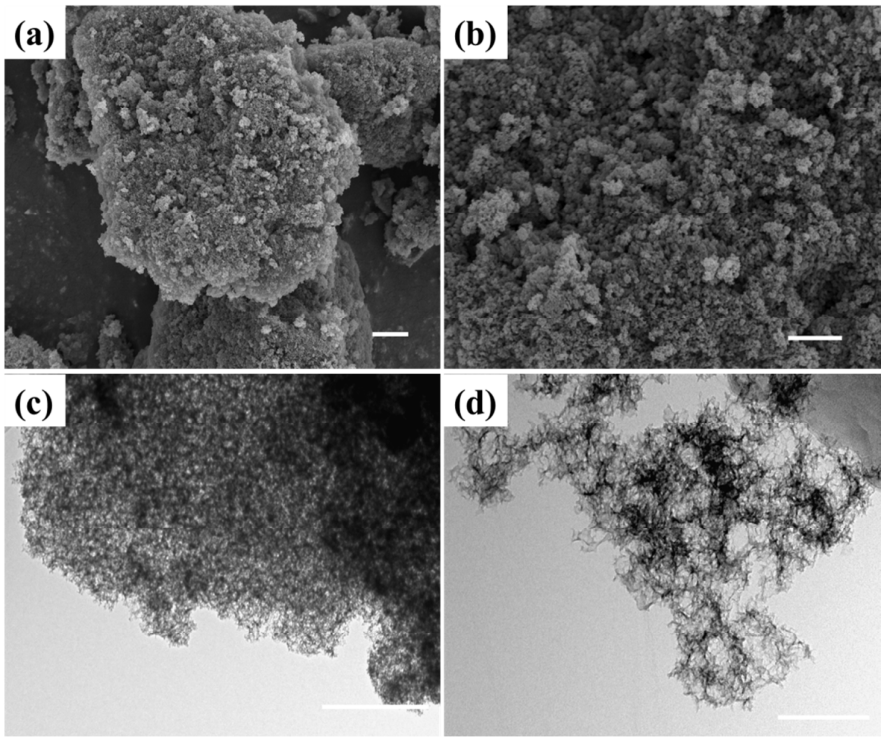

Figure S3. Low (a) and high (b) magnification SEM image of the CN/PC sample; low (c) and high (d) magnification TEM image showing the porous structure of the CN/PC hybrid catalyst. Scale bar: (a)2 μm,(b)1 μm, (c)1 μm, (d)200 nm.

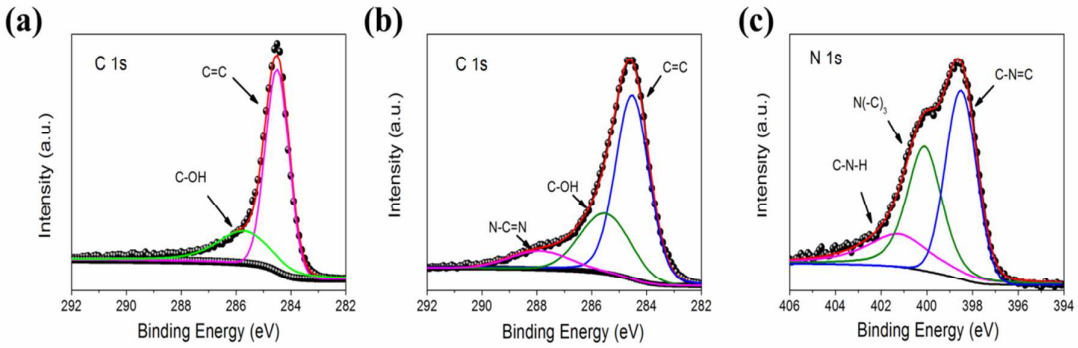

Figure S4. High resolution C 1s XPS spectra recorded from (a) bare PC substrate and (b) the CN/PC catalyst; (c) N 1s XPS spectrum from the CN/PC sample.

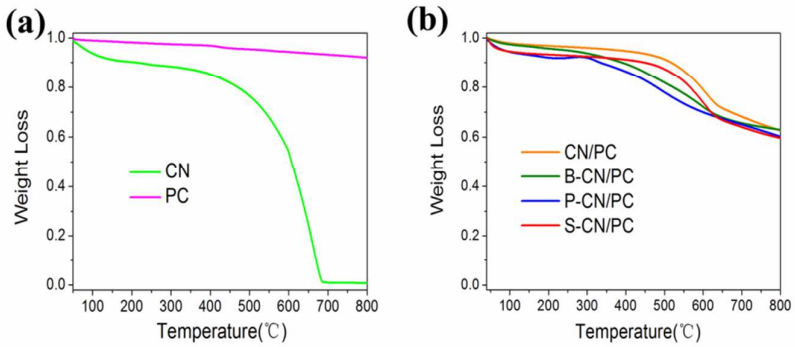

Figure S5. Thermal gravimetric analyses of the weight change of (a) bare CN and PC, (b) X-CN/PC series samples with a ramp rate of 5 °C /min under Ar flow (100 mL/min).

Note: the pure g-C_3N_4 (CN in the figure) starts to sublimation and decompose when temperature is above *ca.* 500 °C, which then loses 100 % weight at 690 °C. The PC carbon, by contrast, is quite stable until 800 °C. The weight percentage of the pristine, B-, P- and S-doped g-C_3N_4 within the hybrids are determined to be 25 wt%, 28 wt%, 22 wt% and 24 wt% respectively. The comparative loading mass of the different g-C_3N_4 species allows a viable comparison study of their electrocatalytic activity.

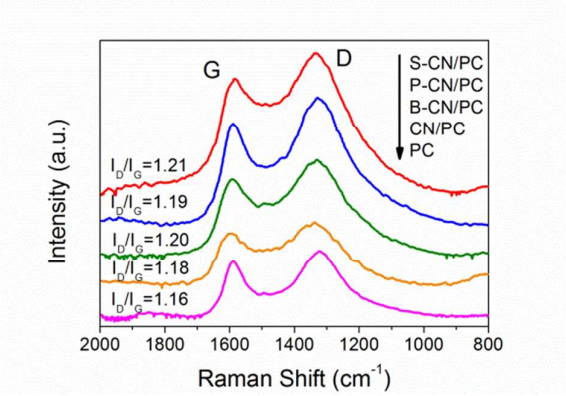

Figure S6. Raman spectra of the X-CN/PC series samples with the bare PC sample as reference. The relatively I_D/I_G ratios are also listed.

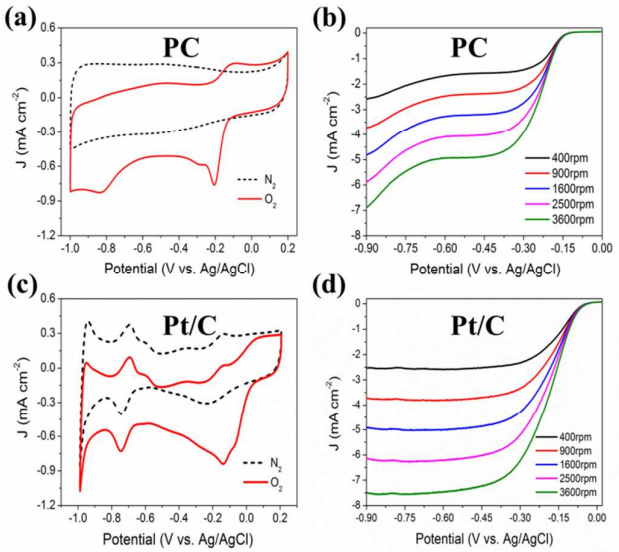

Figure S7. Electrochemical catalytic performance toward ORR in 0.1 M KOH solution of the control samples: CV scans of the bare PC substrate (a) and commercial 20 wt% Pt/C (c) sample; LSV curves of the PC (b) and Pt/C (d) samples at different rotating speeds.

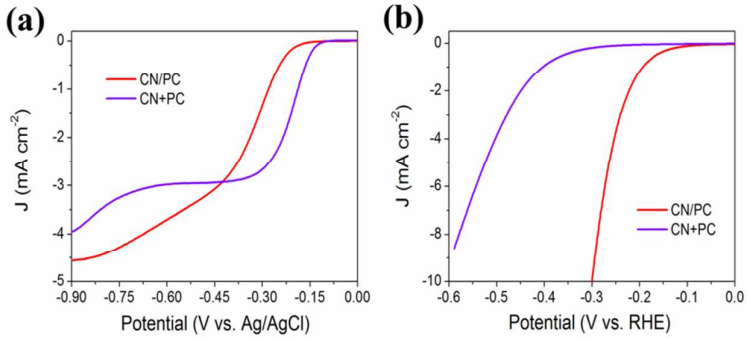

Figure S8. (a) ORR and (b) HER activity comparison of the *in situ* polymerized CN/PC hybrid catalyst and the CN and PC mechanical mixture sample upon the same loading mass. The CN weight percentage was set as 25 wt%, in accordance with that in the CN/PC hybrid sample.

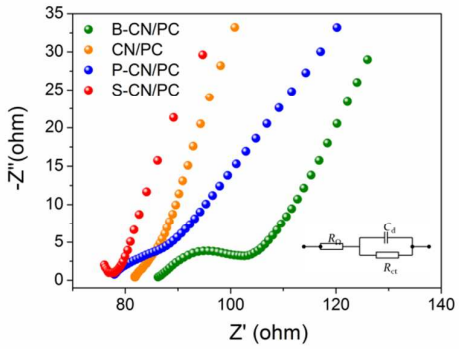

Figure S9. Electrochemical impedance spectroscopy data for the ORR process of different samples; data were collected for the electrodes at -0.3 V (vs. Ag/AgCl) in O_2 saturated 0.1 M KOH, frequency range: 1 Hz to 10^5 Hz; inset is the equivalent circuit.

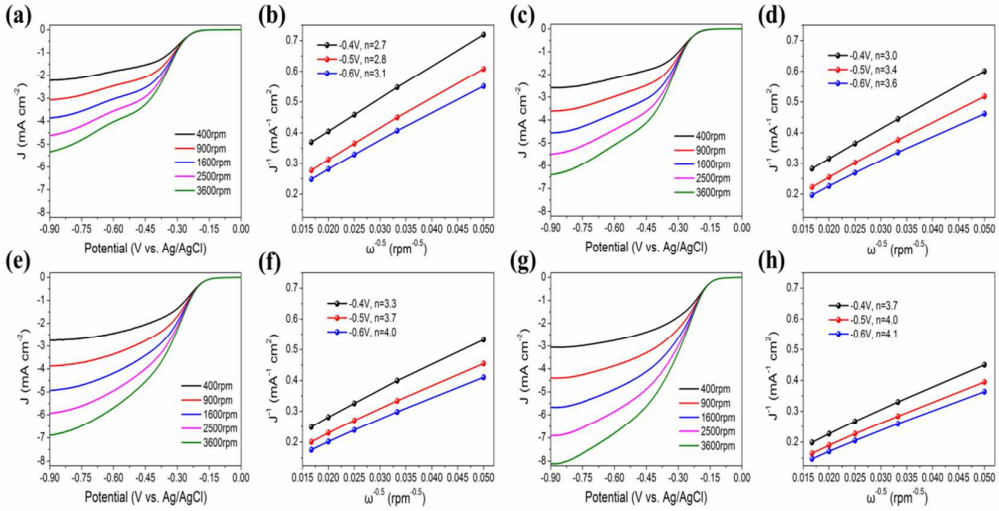

Figure S10. LSV curves at different rotation speeds from 400 to 3600 rpm of (a) B-CN/PC, (c) CN/PC, (e) P-CN/PC, (g) S-CN/PC samples and the Koutecky–Levich plots of (b) B-CN/PC, (d) CN/PC, (f) P-CN/PC and (h) S-CN/PC at different potentials. The corresponding electron transfer numbers (n) are also given.

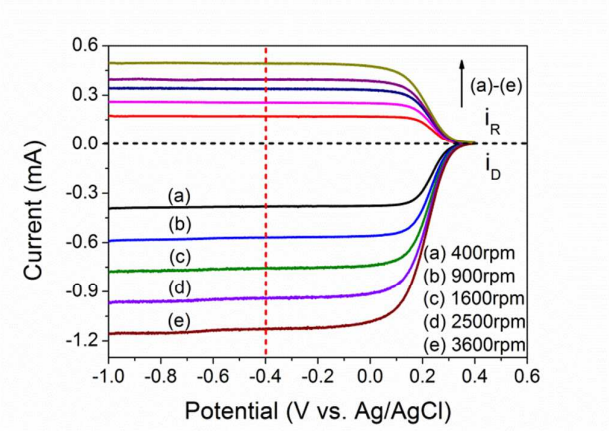

Figure S11. RRDE (Pt ring GC disk electrode) voltammograms for the reduction of $K_3[Fe(CN)_6]$ at the disk electrode in N_2 saturated aqueous KCl solution with disc scan rate of 10 mV s^{-1} at different rotation speeds.

Note: The current collection efficiency (N) of Pt ring in RRDE technique is determined by using single electron reversible couple of ferrocyanide/ferricyanide system.[11] Specifically, a mirror-polished Pt ring GC disk electrode was immersed into N_2 saturated 0.5 M KCl solution containing 10 mM $K_3[Fe(CN)_6]$. The disk electrode was scanned between -1.0 – 0.4 V (vs. Ag/AgCl) at 10 mV s^{-1} and the ring potential was set at 0.5 V. The LSV curves were recorded at rotation speeds of 400-3600 rpm and the ratio the ring and disk limiting currents ($N = i_r/i_d$) reveals the N. In the present system, the N was determined to be 0.44 irrespective of the rotation speed.

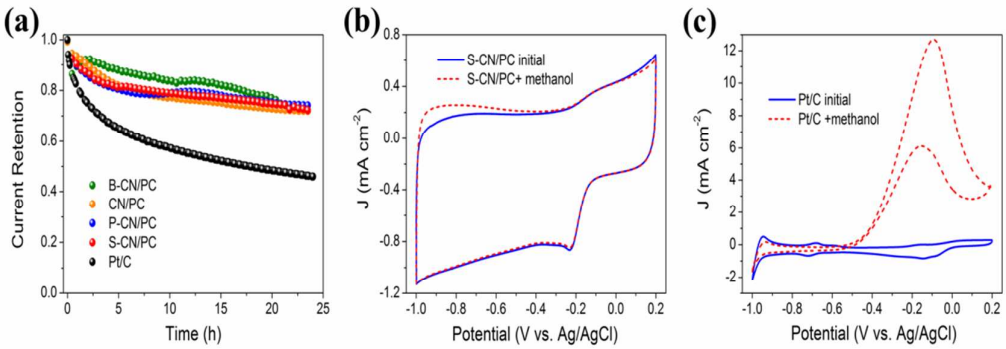

Figure S12. (a) Chronoamperometric durability tests of the X-CN samples and referenced Pt/C sample at 1600 rpm and -0.3 V (vs Ag/AgCl) in O_2 saturated 0.1 M KOH; cross-over tolerance tests of the representative S-CN/PC (b) and Pt/C (c) samples before and after the addition of 10 vol% methanol into the electrolyte. The drastic anodic current of the Pt/C modified electrode suggests the susceptive selectivity of Pt/C catalyst.

Note: In a continuous amperometric i-t test at 1600 rpm and -0.3 V potential, the Pt/C sample loses approximately 54% of its initial current density, whilst all the g-C_3N_4-based samples profile similar but much better stability with reduction current preservation of around 75% (Figure S12a). The improved durability is presumably owing to the high chemical stability of the carbon nitride species and the robustness of the interconnected PC substrate. Moreover, a much enhanced reaction selectivity of the representative S-CN/PC with regard to the referenced Pt/C catalyst is observed in the methanol mixed electrolyte, suggesting the good cross-over tolerance of the metal-free catalyst (Figure S12b, c).

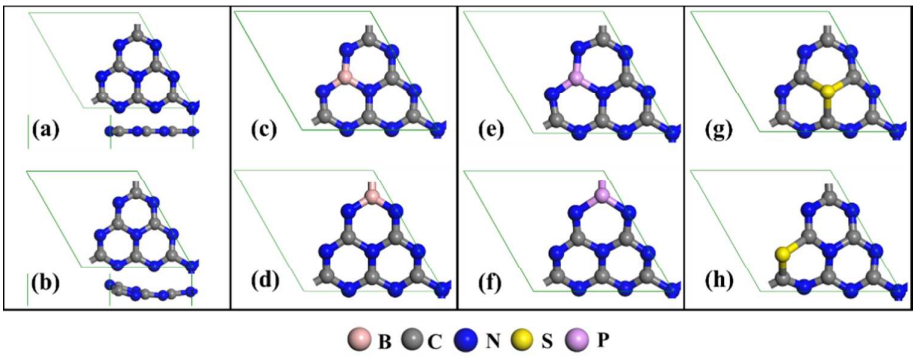

Figure S13. The top views and side views of (a) coplanar and (b) corrugated structures of g-C_3N_4 unit cell. The optimized structures of g-C_3N_4 doping by B (c and d), P (e and f), and S (g and h) atoms, with the dopants replacing the carbon atoms at different positions.

Note: Both the coplanar and corrugated structures of unit cell g-C_3N_4 are shown, whereas the corrugated structure is energetically more stable, thus is adopted as pristine C_3N_4 for the following calculations. In terms of energy per unit cell, the energy of corrugated structure is 0.2 eV lower than that of coplanar structure.

Based on our experimental findings and other groups' works,[12-15] we constructed six structures by doping g-C_3N_4 with boron, phosphorous, and sulfur atoms. In Figure S13, (c) and (e) are corner-carbon replaced doping; (d) and (f) are bay-carbon replaced doping; (g) is graphitic nitrogen replaced doping and (h) is pyridinic nitrogen replaced doping. Interestingly, all the six doped structures have extra one unpaired electron caused by the doping, giving a doublet spin multiplicity. As to the stability, we found that it is more favorable if boron or phosphorus atom replaces the bay-carbon, and sulfur atom replaces the pyridinic nitrogen. Thus, we would select (d), (f), (h) as B-doped, P-doped, and S-doped C_3N_4 for following calculations. Note that all the structures favor corrugated configurations to avoid the electron lone pair interactions between the N atoms.

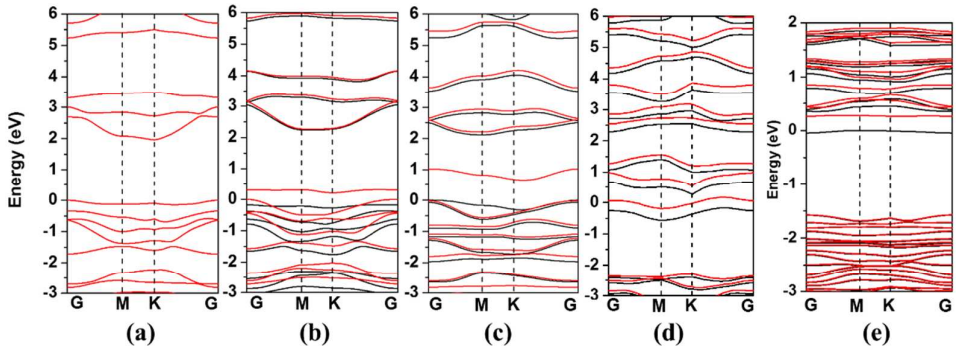

Figure S14. Band structures of (a) pristine, (b) B-doped, (c) P-doped, (d) S-doped and (e) S-doped C_3N_4 with lower doping concentration. The Fermi level was set at 0.

Note: The red bands and black bands here represent the spin up and spin down electrons separately. All the computations are first based on an identical dopant concentration of 7.14 at%, which corresponds to one dopant in a supercell. As shown above, the band gaps of pristine, B-, P-, and S-doped C_3N_4 are 1.95, 0.21, 0.66 and 0.10 eV, respectively. For clarifying the potential impact of heteroatom concentration distinctions, we also examined the model of S-doped C_3N_4 with different S concentrations. When decreasing the doping concentration from 7.14 at% to a much lower value of 1.78 at%, the band gap of the S-CN sample only shows a small change from 0.10 eV to 0.26 eV, yet both are remarkably smaller than that of the pristine CN sample (1.95 eV).

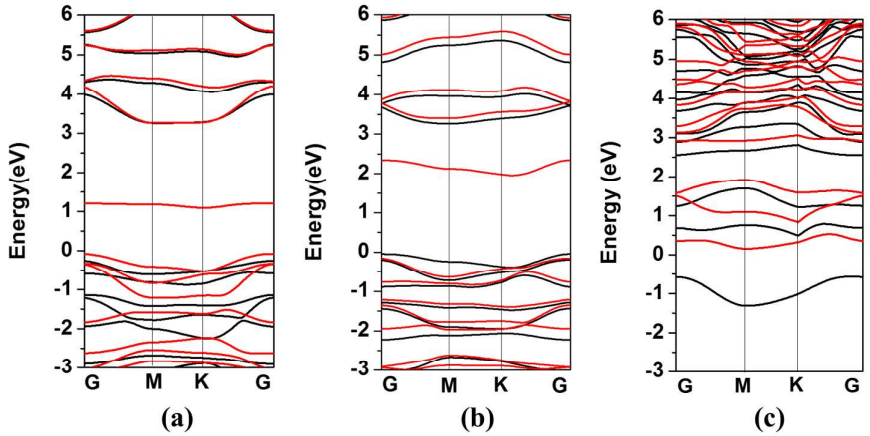

Figure S15. Band structures of (a) B-doped, (b) P-doped, (c) S-doped C_3N_4 calculated by HSE06 functional. We set the Fermi level at 0. The red bands and black bands here represent the spin up and spin down electrons separately. The band gaps of B-doped, P-doped and S-doped C_3N_4 are 1.17, 2.00, and 0.74 eV, respectively.

Note: We realized that the band gaps calculated using GGA-PBE functional are generally underestimated.[16] For example, the experimental band gap of condensed graphitic carbon nitride (g-C_3N_4) is about 2.7 eV, investigated by Wang *et al.*[17] However, our PBE calculation shows a smaller band gap of 1.95 eV. To solve this problem, we further employed HSE functional, which has been proven to well describe the band gaps,[18] to re-evaluate the band gap values.

According to our HSE calculation, the pristine g-C_3N_4 has a large band gap about 3.16 eV, which is much larger than our PBE result and very close to the experiment value. Thus, HSE functional was also applied to calculate the band gaps of B-doped, P-doped and S-doped C_3N_4 monolayers, as shown in Figure S15. Compared with our PBE results in Figure S14, all the band gaps are enlarged prominently.

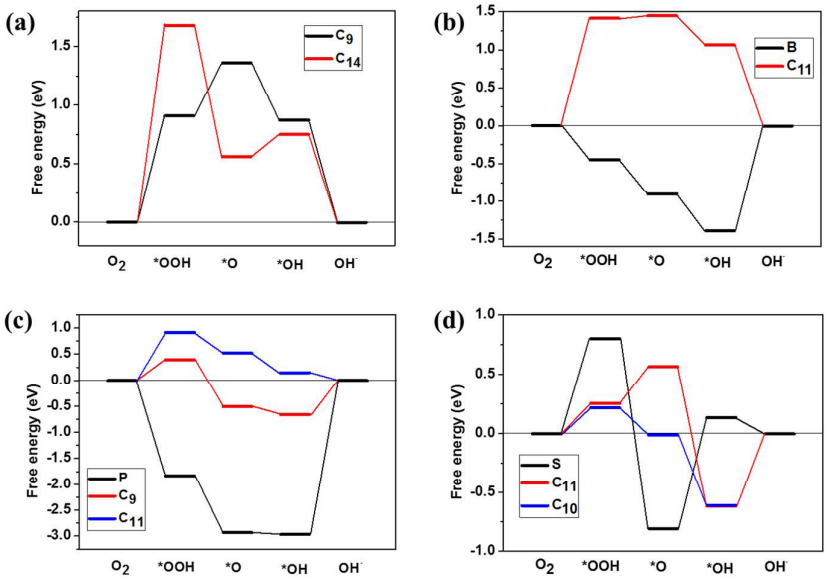

Figure S16. Free energy diagrams of each reaction step on (a) pristine, (b) B-doped, (c) P-doped and (d) S-doped C_3N_4, at the equilibrium potential $U^0 = 0.46$ V. The lines of different colors represent the reactions on different active sites, and free energy diagram of the best active site for each doped C_3N_4 would show in Figure 5.

Note: For (a) pristine C_3N_4, C_9 and C_{14} are considered, as they are different kinds of carbon atoms. Owing to the highest energy barrier of the first step on C_{14} (a, red line), C_9 is thought to be the real active site of pristine C_3N_4. The most sluggish step on C_9 is also the first step, with an energy value of 0.91 eV.

As to B-doped C_3N_4 (b), it seems that B atom has large attractions to O-containing species accounting for the negative value of the reaction free energies shown by black line. B atom is proved to be the real active site of B-doped C_3N_4, with an energy barrier of 1.39 eV at the last step, while reaction on C_{11} has a larger energy barrier of 1.41 eV at the first step (b, red line). Hereby, we omitted the reaction pathway of C_9 because of the very bad results.

Different from B-doped C_3N_4, the real active sites of P-doped, and S-doped C_3N_4 are not the dopants. It is C_9 of P-doped C_3N_4 that shows a relatively small energy barrier of 0.66 eV at the last step (c, red line). For other calculated potential active sites, the energy barriers are larger, especially for P atom owing to its strong attraction to O-containing species.

Impressively, two real active sites of S-doped (C_{10} and C_{11}) are confirmed by our calculations, as shown in (d) by blue and red lines. Red line has three uphill, except for its third step, while blue line has two uphill at its first and fourth steps. However, the most sluggish step of these two lines is the same one, *i.e.*, the last step forming hydroxide anion. Additionally, the largest energy barrier is 0.61 eV, much lower than the energy barrier saw on black line (S atom as potential active site).

Thus, only the active sites with best performances are shown in Figure 5, while only one real active site of S-doped C_3N_4 is illustrated in Figure 5 to simplify.

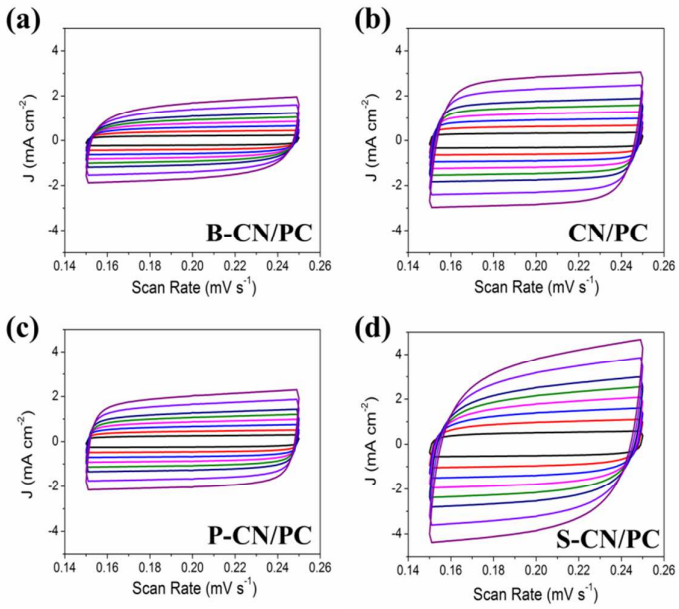

Figure S17. CV curves of different samples recorded in an overpotential window between 0.15 and 0.25 V (vs. RHE) at scan rates from 20 to 200 mV s^{-1}.

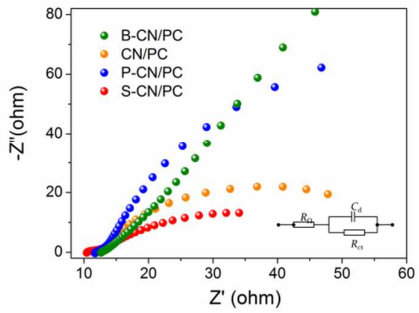

Figure S18. Electrochemical impedance spectroscopy data for HER process of different catalysts; data were collected for the electrodes under HER overpotential of 200 mV in N_2 pruged 0.5 M H_2SO_4, frequency range: 1 Hz to 10^5 Hz; inset is the equivalent circuit.

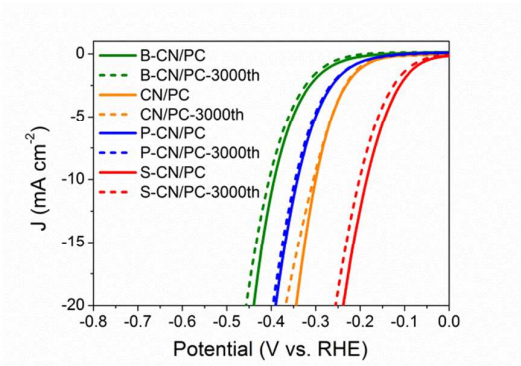

Figure S19. Durability tests of different catalysts. All the catalysts show only slight decay after 3000 cycles at 100 mV s^{-1} from -0.4 to 0.2 V (vs. RHE).

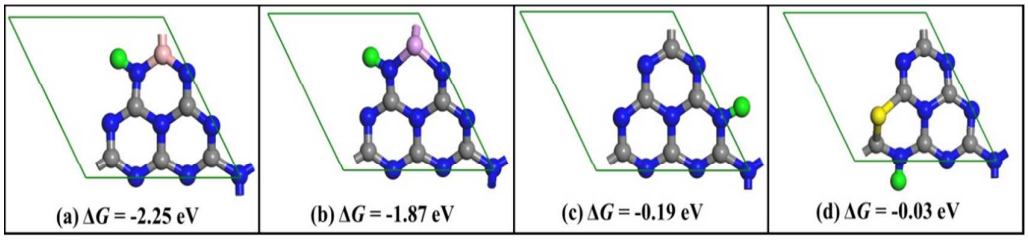

Figure S20. The computed Gibbs free energies (ΔG) of the most favorable HER on (a) B-, (b) P-, (c) pristine, and (d) S-doped C_3N_4. The green balls are hydrogen atoms.

Table S1 Porous structural characteristics of different samples

Sample	S_{BET}	S_{micro}	V_{tol}	V_{micro}
	$m^2 g^{-1}$		$cm^3 g^{-1}$	
Bare Porous carbon	758.4	169.3	2.3153	0.0787
CN/PC	394.6	35.5	1.1691	0.0140
B-CN/PC	185.4	6.1	0.6339	0.0009
P-CN/PC	312.3	10.5	0.9635	0.0017
S-CN/PC	470.8	92.0	1.3210	0.0495

Table S2. Hirshfeld charges and spin densities of the atoms numbered as 7 to 14 in different structures

	pristine C_3N_4		**B-doped C_3N_4**			**P-doped C_3N_4**			**S-doped C_3N_4**		
		charge		charge	spin		charge	spin		charge	spin
7									S	0.118	0.098
9	C	0.172	C	0.164	0.028	C	0.165	0.022	C	0.095	0.107
10	C	0.169	C	0.164	0.024	C	0.165	0.022	C	0.154	0.035
11	C	0.170	C	0.167	0.009	C	0.168	0.005	C	0.134	0.131
12	C	0.172	C	0.173	0.005	C	0.155	0.018	C	0.089	0.129
13	C	0.171	B	0.180	0.017	P	0.408	0.472	C	0.148	0.089
14	C	0.174	C	0.173	0.005	C	0.155	0.018	C	0.142	0.100

Here is the calculated positive Hirshfeld charges and spin densities of carbon atoms and dopants. Simply, we denoted the largest charge and spin density of carbon atom by red rectangle. These denoted carbon atoms and dopants (red letters) are considered as potential active sites. In the system of pristine C_3N_4, C_9 is also included, because C_9 is quite different from C_{14}, considering their chemical environments.

Table S3. Comparison study of ORR performance of different metal-free catalysts in 0.1 M KOH

Catalyst	Onset Potential (V)	Electron transfer number (n)	HO_2^- yield	Reference
C_3N_4@CMK-3	~ 0.1 (vs. Ag/AgCl)	~4.0	-	J. Am. Chem. Soc. **2011**, 133, 20116
Macroporous C_3N_4@C	-0.14 (vs. Ag/AgCl)	~3.0	< 50%	Angew. Chem. Int. Ed. **2012**, 51, 3892
N-doped Graphene Framework	-0.18 (vs. Ag/AgCl)	3.7	< 20%	Angew. Chem. Int. Ed. **2012**, 51, 11371
S,N co-doped Mesoporous Graphene	-0.06 (vs. Ag/AgCl)	3.3-3.6	< 35%	Angew. Chem. Int. Ed. **2012**, 51, 11496
P-doped Graphene	0.92 (vs. RHE)	3.0-3.8	< 50%	Adv. Mater. **2013**, 25, 4932.
s-g-C_3N_4@GQD	-0.07 (vs. Ag/AgCl)	~3.5	< 30%	J. Mater. Chem. A, **2015**, 3, 1841
3D N-doped Garphene Nanoribbons	-0.05 (vs. Ag/AgCl)	3.71-3.96	< 14.7%	Small **2015**, 11, 1423
N-doped Porous Carbon Superstructures	-	~3.20-3.94	< 20%	Adv. Mater. **2016**, 28, 1981
N,P-codoped CNT/graphene hybrid	0.94 (vs. RHE)	~3.88-4.0	< 6%	Adv. Mater. **2016**, 28, 4606
CN/PC	-0.14V (vs. Ag/AgCl)	3.25-3.64	< 38%	This work
B-CN/PC	-0.17 V (vs. Ag/AgCl)	3.11-3.40	< 45%	This work
P-CN/PC	-0.1 V (vs. Ag/AgCl)	3.55-3.78	< 23%	This work
S-CN/PC	-0.07 V (vs. Ag/AgCl)	3.74-3.89	< 13%	This work

Table S4. Comparison study of HER performance of different catalysts in 0.5 M H_2SO_4

Catalyst	Loading Mass ($\mu g\ cm^{-2}$)	Onset Potential (mV vs. RHE)	η @ 10 mA cm^{-2} (mV vs. RHE)	Tafel Slope ($mV\ dec^{-1}$)	J_0, geometric ($\mu A\ cm^{-2}$)	Reference
MoO_3-MoS_2 Nanowires	60	-(150-200)	~ -250	50-60	0.082	Nano Lett. **2011**, 11, 4168.
MoS_2 Nanosheets	285	-120	~ -180	50	8.9	Adv. Mater. **2013**, 25, 5807.
Co-NRCNTs	280	-50	-260	80	10	Angew. Chem. Int. Ed. **2014**, 53, 4372
N/Co-doped PCP//NRGO	357	-58	-229	126	-	Adv. Funct. Mater. **2015**, 25, 872.
Porous Co-N-C	2000	-20	-133	57	70	Nature Comm. **2015,** 6, 7992
Textured MoS_2 Microflakes	-	~-100	-174	63	19	Nano Lett. **2016**, 16, 4047.
N,P-doped Graphene	200	-290	-420	91	0.24	ACS Nano, **2014**, 8, 5290.
C_3N_4@NG	~100	-	-240	51	0.35	Nature Comm. **2014**, 5, 3783.
g-C_3N_4 Nanoribbon-G	143	-80	-207	54	39.8	Angew. Chem. Int. Ed. **2014**, 126, 14154.
g-C_3N_4@S-Se-pGr	280	-92	-300	86	6.27	J. Mater. Chem. A, **2015**, 3, 12810.
N,S-doped Graphene 500C	-	-130	-276	81	8.4	Angew. Chem. Int. Ed. **2015**, 54, 2131.
CN/PC	280	-167	-300	100	11.3	This work
B-CN/PC	280	-254	-405	93	0.8	This work
P-CN/PC	280	-201	-343	100	4.8	This work
S-CN/PC	280	-55	-186	84	13.8	This work

References SI

1. Delley, B. An All‐Electron Numerical Method for Solving the Local Density Functional for Polyatomic Molecules. *J. Chem. Phys.* **1990**, 92, 508-517.

2. Delley, B. From Molecules to Solids with the $DMol^3$ Approach. *J. Chem. Phys.* **2000**, 113, 7756-7764.

3. Grimme, S. Semiempirical GGA‐Type Density Functional Constructed with A Long‐Range Dispersion Correction. *J. Comput. Chem.* **2006**, 27, 1787-1799.

4. Perdew, J. P.; Burke, K.; Ernzerhof, M. Generalized Gradient Approximation Made Simple. *Phys. Rev. Lett.* **1996**, 77, 3865.

5. Klamt, A.; Schüürmann, G. COSMO: A New Approach to Dielectric Screening in Solvents with Explicit Expressions for the Screening Energy and its Gradient. *J. Chem. Soc., Perkin Transactions 2* **1993**, 799-805.

6. Hirshfeld, F. L. Bonded-Atom Fragments for Describing Molecular Charge Densities. Theoretical Chemistry Accounts: Theory, Computation, and Modeling*, Theoretica Chimica Acta,* **1977**, 44, 129-138.

7. Nørskov, J. K.; Bligaard, T.; Logadottir, A.; Kitchin, J.; Chen, J.; Pandelov, S.; Stimming, U. Trends in the Exchange Current for Hydrogen Evolution. *J. Electrochem. Soc.* **2005**, 152, J23-J26.

8. Nørskov, J. K.; Rossmeisl, J.; Logadottir, A.; Lindqvist, L.; Kitchin, J. R.; Bligaard, T.; Jonsson, H. Origin of the Overpotential for Oxygen Reduction at A Fuel-Cell Cathode. *J. Phys. Chem. B* **2004**, 108, 17886-17892.

9. Weast, R. C. *Handbook of chemistry and physics, 49th Edition.* Cleveland, OH: Chemical Rubber Company*,* **1969**.

10. Ge, X.; Sumboja, A.; Wuu, D.; An, T.; Li, B.; Goh, F. T.; Hor, T. A.; Zong, Y.; Liu, Z. Oxygen Reduction in Alkaline Media: from Mechanisms to Recent Advances of Catalysts. *ACS Catal.* **2015**, 5, 4643-4667.

11. Hancock, C. A.; Ong, A. L.; Slater, P. R.; Varcoe, J. R. Development of $CaMn_{1-x}Ru_xO_{3-y}$ (x= 0 and 0.15) Oxygen Reduction Catalysts for Use in Low Temperature Electrochemical Devices Containing Alkaline Electrolytes: *Ex Situ* Testing Using the Totating Ring-Disk Electrode Voltammetry Method. *J. Mater. Chem. A* **2014**, 2, 3047-3056.

12. Zhang, Y.; Mori, T.; Ye, J.; Antonietti, M. Phosphorus-Doped Carbon Nitride Solid: Enhanced Electrical Conductivity and Photocurrent Generation. *J. Am. Chem. Soc.* **2010**, 132, 6294-6295.

13. Gang, C.; Shang-Peng, G. Structure and Electronic Structure of S-Doped Graphitic C_3N_4 Investigated by Density Functional Theory. *Chin. Phys. B* **2012**, 21, 107101.

14. Wang, Y.; Li, H.; Yao, J.; Wang, X.; Antonietti, M. Synthesis of Boron Doped Polymeric Carbon Nitride Solids and Their Use as Metal-Free Catalysts for Aliphatic C–H Bond Oxidation. *Chem. Sci.* **2011**, 2, 446-450.

15. Liu, G.; Niu, P.; Sun, C.; Smith, S. C.; Chen, Z.; Lu, G. Q.; Cheng, H.-M. Unique Electronic Structure Induced High Photoreactivity of Sulfur-Doped Graphitic C_3N_4. *J. Am. Chem. Soc.* **2010**, 132, 11642-11648.

16. Filippi, C.; Singh, D. J.; Umrigar, C. J., All-Electron Local-Density and Generalized-Gradient Calculations of the Structural Properties of Semiconductors. *Phys. Rev. B* **1994**, 50, 14947.

17. Wang, X.; Maeda, K.; Thomas, A.; Takanabe, K.; Xin, G.; Carlsson, J. M.; Domen, K.; Antonietti, M., A Metal-Free Polymeric Photocatalyst for Hydrogen Production from Water under Visible Light. *Nat. Mater.* **2009**, 8, 76-80.

18. Heyd, J.; Scuseria, G. E.; Ernzerhof, M., Hybrid Functionals Based on A Screened Coulomb Potential. *J. Chem. Phys.* **2003**, 118, 8207-8215.